Experimental study of resonance-induced coherent spin current in thin FM/NM bilayers

As part of the 7th School of Advanced Experimental Physics
Brazilian Center for Research in Physics (CBPF)

E. Aguero,[*] I. V. L. F. Andrade,[†] M. E. Ramos Pedro,[‡] G. T. Mizumura,[§] G. J. N. Soares,[†] and D. Vasquez[¶]

(Dated: March 20, 2024)

Spintronic devices use charge and spin currents of electrons to transport information, harnessing numerous advantages when compared to conventional electronics that produce high heat and are close to their quantum limit. In this study, multiple thin film bilayers were deposited to test their suitability to transport spin current using magnetron sputtering, ferromagnetic resonance, and the inverse spin Hall effect. Among the combinations studied, the YIG/Pt bilayer was the most promising, as YIG has magnetic and insulating properties, whereas the big atomic number, total angular momenta and its spin-orbit coupling constant of platinum explains its good performance. Additionally, X-ray reflectivity and X-ray Photoelectron Spectroscopy were employed to assess thickness and oxidation levels of the films.

I. INTRODUCTION

The dynamics of magnetization in ferromagnetic materials are described by the Landau-Lifshitz-Gilbert equation [1].

$$\frac{d\boldsymbol{m}}{dt} = -\gamma\boldsymbol{m}\times\boldsymbol{H} + \alpha\boldsymbol{m}\times\frac{d\boldsymbol{m}}{dt} \qquad (1)$$

Here, $\boldsymbol{m}$ is the magnetization vector inside the material, γ is the gyromagnetic ratio of the electron, and $\boldsymbol{H}$ is the magnetic field in the material. The first term in the right-hand side of equation 1 corresponds to an oscillating, undamped precession around the magnetic field, whereas the second term corresponds to a dissipative, damping precession of the magnetization vector. The Gilbert damping coefficient α is proportional to this energy dissipation. The natural precession frequency of the system is given by the Larmor frequency $\omega = \gamma H$ [1].

A. Spin pumping

Spin pumping occurs at the interface of a ferromagnetic/normal metal (FM/NM) bilayer and involves the transfer of angular momenta from one material to the other. The necessary condition for spin pumping is a temporal variation in the magnetization of the FM. Experimentally, one way to obtain this condition is when the magnetic material is in a ferromagnetic resonance (FMR), which is obtained by subjecting the FM material to a constant magnetic field and a perturbative, perpendicular AC magnetic field equal to the Larmor frequency,

---

* ILACVN, Universidade Federal da Integração Latino-Americana.
† UFRJ, Universidade Federal do Rio de Janeiro.
‡ UFSC, Universidade Federal de Santa Catarina.
§ UNICAMP, Universidade Estadual de Campinas.
¶ Universidad Nacional de Ingenieria, Peru.

oscillating typically in the order of radiofrequency (RF). This RF competes with the dissipation term in (1), cancelling its damping effect exactly at its resonance frequency. Thus, by measuring the RF absorption in the vicinity of the resonance condition, one can obtain the Gilbert damping coefficient of the FM material. [2]

It has been observed that the dissipation Gilbert coefficient of the combined FM/NM is enhanced when compared to the thin FM layer [3]. Numerous theoretical frameworks have been devised to explain this enhanced damping mechanism [3, 4], the dominating one being the existence of transfer of angular momenta from the FM material to the NM material induced by a chemical potential difference in the interface between the two layers [5]. To quantify the spin pumping, one can use the enhancement of the Gilbert damping coefficient, which can be determined by comparing the damping of the multilayer film to the FM substrate, given by

$$\alpha_{SP} = \alpha_{FM/NM} - \alpha_{FM} \qquad (2)$$

In this study, the Gilbert damping of several samples was evaluated through the ferromagnetic resonance measurements at different frequencies. The damping value was obtained from the slope of the linear relationship between the FMR line width and the RF frequency.

B. Direct and Inverse Spin Hall Effect

To measure the material spin current (J_s) and identify if it is promising to be utilized in the area of spintronics, the Spin Hall Effect (SHE) can be applied. This important phenomenon involves the application of an electric current (J_c) composed of electrons, that have charge and spin, onto the nonmagnetic material, to generate a spin current in a transversal direction to the applied current. The spin current can be observed due to the asymmetrical scatter of the electrons with different spin orientations present on the electric current due to the presence of the

spin-orbit coupling interaction in the material. The electron path is determined according to the spin upwards or downwards direction. The spin-up tends to scatter in an opposite direction that the spin-down. This difference in the spin final destiny on the material generates a spin current. However, the signal of J_s has low intensity and high noise levels, compared to the equipment noise levels therefore, requiring a high-precision measurement instrument.

In this perspective, as a solution to the limitations observed in the spin Hall effect, the inverse spin Hall effect emerges. The key distinction lies in how the iSHE operates: in contrast to the conventional SHE, the iSHE induces a spin current to generate a charge current, allowing the measurement of J_s through a thermodynamically reciprocal mechanism, as demonstrated in Fig. 1.

To achieve this, a spin current is injected into the nonmagnetic material through the use of a magnetic material in the resonance condition, which allows the major passage of current due to the increase of the spin pumping phenomenon. In addition, the interaction of this spin current in the NM material is influenced by the presence of a magnetic field (H), that results in a preferential polarization of the FM material spin, leading to a higher concentration in one spin's direction. Consequently, upon encountering the NM material, the electrons will exhibit preferential scattering toward one extremity, resulting in a greater spin accumulation in that region. In this way, as the spin is associated with the electrons and their charge, it effectively is possible to say that there will be a higher accumulation of charge in one of the material sides, which creates the conditions for the observation of an electric potential difference and its measurement.
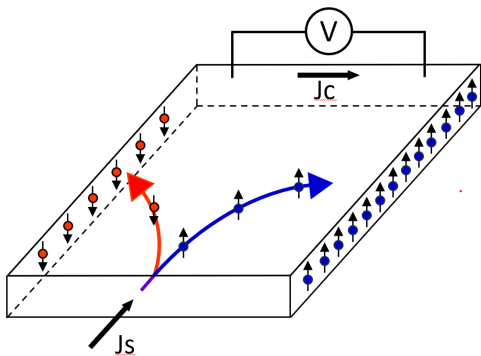

FIG. 1: The operational mechanism of inverse spin Hall effect. A spin-polarized current (Js) is injected into the material and asymmetrically scattered, resulting in a charge current (Jc) by the charges accumulation at the extremities of the NM material.

Therefore, when conducting an experimental measurement of iSHE, it is possible to identify the electric potential difference at the moment of resonance.

II. EXPERIMENTAL METHODOLOGY

A. Samples

For the conducted studies, primarily a specific ferromagnetic material was chosen, a conductor alloy of $Ni_{80}Fe_{20}$, known as Permalloy (Py), due to its low damping, low cost, easy fabrication, volume of studies, and literature data. On the other side, as nonmagnetic metallic materials, Platinum (Pt), Copper (Cu), Titanium (Ti), and Tungsten (W) were selected due to their conductivity. For its deposition, the thickness of 30 nm was chosen for the Py, and it was deposited above a thin Si/SiO2 (100) substrate, which provides a great ordination of the material layers. On the other hand, for the nonmagnetic materials, the thickness of 6 nm was chosen, as it is observed in the literature from larger thicknesses than this that the spin pumping phenomenon is hampered due to the start of the disorder of the spin.

Subsequently, the experimental results with Py were evaluated and the two most promising nonmagnetic materials coupled to Py were deposited, with a 6 nm layer thickness, above thin films of Yttrium Iron Garnet or YIG (111), with the chemical composition of $Y_3Fe_5O_{12}$. This oxide was sputtered above a lithographed area in a substrate of Gadolinium Gallium Garnet or GGG (111), which provides a good crystallographic orientation for the YIG.

The deposition above different ferromagnetic materials aims to compare the spin pumping and spin Hall effect in materials with different properties of conductivity, because, unlike Py, which is conductive, the YIG is an insulator. The materials choice and their effects will be discussed in the results section.

B. Magnetron Sputtering

The magnetron sputtering technique was used for the thin film deposition on the nanometer scale.

For the sample preparation, the substrates were cleaned by ultrasound, followed by drying in compressed air. Next, the dry substrate was fixed with carbon tape in the sample holder and then directed and positioned in the smaller chamber (load-lock) of the equipment. Therefore, once the sample is inside the equipment and the cap of the smaller chamber is closed, the vacuum system is turned on, striving to equalize the pressure with the main chamber. When a similar pressure condition is achieved, the bridge between the two chambers is opened and the sample is directed to the main chamber through an operator arm, where the sample is positioned with the raising of the inner sample holder. After this, the passage between the chambers is closed. Then, the sample holder is lowered until it is just 10 centimeters above the targets, and the sample is guided by the commands in the software to move above the target of interest.

The equipment functionality is based primarily on the application of a high vacuum condition in the main chamber, to develop a free particle atmosphere and minimize any interference that could happen at the moment of deposition.
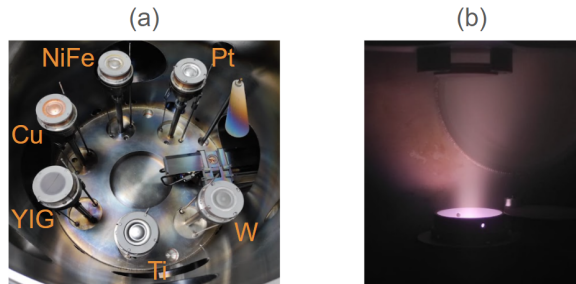

FIG. 2: Photos of magnetron sputtering on the inside. In (a) the targets that were used to fabricate the thin films. In (b) the generated plasma of the deposition process.

In the main chamber, an inert atmosphere composed of Argon gas is applied, which is ionized when subjected to an electric potential difference. With the opening of the chosen target shutter, the Argon's plasma concentrates on its surface, as a result of the presence of a magnet on the target, as observed in Fig. 2. In this way, the Argon ions collide with the target with enough kinetic energy to sputter the atoms of the material's surface, making these atoms spread in the chamber. By convenience, the sputtered atoms deposit in the substrate, creating a thin film, where its thickness is controlled by the combination of the material deposition rate and the time of the procedure. The deposited samples above the Si/SiO2 are demonstrated in the Fig. 3.
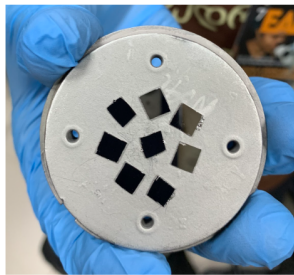

FIG. 3: Samples of Py thin films deposited on Si (100) substrates.

C. X-ray Reflectivity (XRR)

The X-ray reflectivity (XRR) technique was employed to analyze the thickness and deposition rate of several samples.

To prepare the samples, they were fixed in the sample holder by the use of modeling clay and positioned firmly,

with the help of a glass cleaned with isopropyl alcohol, and directed to the equipment. Two Permalloy samples and a Platinum calibration sample were analyzed as control samples, to learn about the technique and confer if the rate of deposition was precisely determined.

The equipment operates based on the principle of X-ray incidence on the sample at various angles, allowing, in this way, the scanning and acquisition of information. This material property is significant because it determines whether the X-rays are reflected or can penetrate the thin film surface. When the film refracts it, the beam encounters the substrate, where it reflects and is captured by the detector.
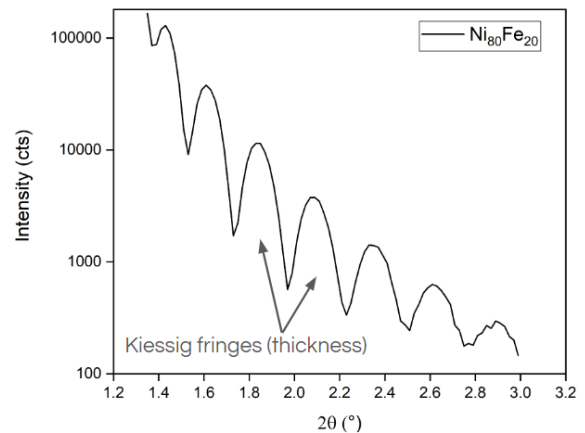

FIG. 4: Kiessig fringes pattern for a Py sample, which confirms the thickness of approximately 30 nm.

The difference between the received signals, of the film reflection and the substrate reflection, by the detector, generates a pattern that can be observed in the graphic of Fig. 4, named by Kiessig fringes. With this pattern, it's possible to extract data about the thickness of the material in correlation, and with the time of deposition as an input parameter is possible to obtain the confirmation of the deposition rate.

D. Ferromagnetic Resonance (FMR)

The Ferromagnetic Resonance (FMR) experiment aims to analyze the absorption of the radiofrequency (RF) after passing through the sample when the condition of resonance of ferromagnetic is satisfied [6].

The measurement procedure of the ferromagnetic resonance spectra used in our experiment is fixing the frequency of the RF (ω_{RF}) and varying the intensity of continuous (DC) magnetic field (H_0) applied around the resonance magnetic field (H_{res}). Another possible method is varying the frequency, while the DC magnetic field is maintained fixed.

The experimental configuration is shown in Figure 5, and to explain the measurement procedure we present in Figure 6 a schema of the FMR experiment. The

computer controls many components of the experiment, like the DC power supply (Kepco BOP 40-50M), the radiofrequency (RF) generator (Anritsu model MG3692C) and the alternating current (AC) wave generator (Agilent model 3322OA). The DC power supply will generate a DC magnetic field H_0 in the external coils represented in Figure 6 as red cylinders. The RF generator produces a RF wave that will be partially absorbed by the sample in the condition of resonance and the AC wave generator will create a modulation field H_{mod} in the internal coils represented in Figure 6 as orange cylinders.
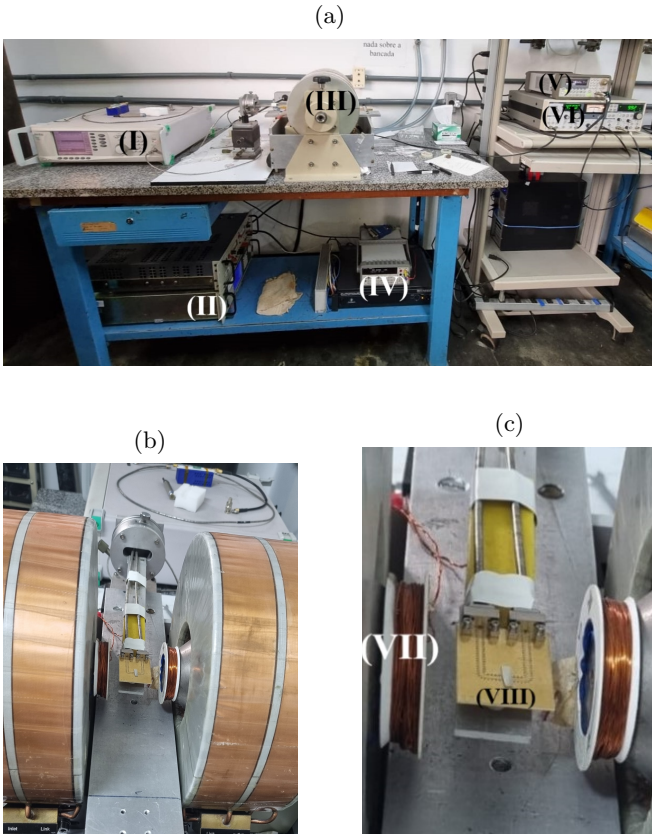
(a)

(b)

(c)

FIG. 5: The experimental configuration of the ferromagnetic resonance (FMR). In (a) there is the radiofrequency (RF) generator (I), the power supply (II), the electromagnetic (III), the power amplifier with the multimeter (IV), wave generator (V), and the lock-in amplifier (VI). In (b) is the lateral vision of the electromagnetic where there are the modulation coils (VII) and the coplanar waveguide (VIII) seen in (c).

The RF wave is guided to the sample by a coplanar waveguide that allows a large bandwidth between 1 GHz and 20 GHz, and the RF not absorbed by the sample was directed to the rectifier diode for converting the AC signal to the DC signal and then measured in the lock-in amplifier. Then, the output signal provided by the lock-in amplifier is converted into a digital using an analog-digital converter (DAC) and recorded and stored on the
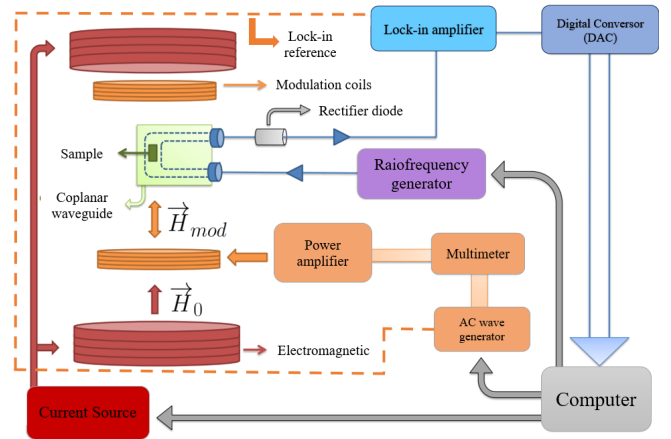

FIG. 6: Schematics of the experimental setup. Extracted from Torrão, (2019) [2].

computer.

The lock-in amplifier (SR124 Analog of the brand Stanford Research Systems) is used because the signal of the FMR experiment is small and may be smaller than the noise of the experiment. The principle of function of the lock-in amplifier is to use a reference frequency to only detect the signal with the reference frequency and filter the other frequencies.

The output of the amplifier is a DC voltage (V_{DC}) which is the mean of the product integrated in the time between the signal of the sample V_{ent} and the signal of reference, for sinusoidal signal [7]:

$$V_{DC} = \frac{1}{T} \int_{t-T}^{t} V_L sin\left(2\pi f_{ref} \cdot s\right) V_{\text{ent}}(s) ds \qquad (3)$$

where T is the time of the integration, V_{L} is the amplitude of reference and the f_{ref} is the frequency of the reference. In our experiment, a sinusoidal signal with $V_{\text{L}} = 500$ mV and $f_{\text{ref}} = 45$ kHz was used. To generate the modulation field, a pair of Helmholtz coils with 2 cm in diameter were used fed by a wave generator in conjunction with a power amplifier with 0.86 V for YIG resulting in a $H_{\text{AC}} = 0.5$ Oe, and 2.18 V for Permalloy (Py) resulting in a $H_{\text{AC}} = 1.3$ Oe.

The field modulation with Helmholtz's coils (H_{AC}) is important to reduce the noise of the signal but changes the shape of the spectrum, as seen in Figure 7, which is described by Eq. 3 as the derivative of Lorentzian using numerical methods. Then, to fit the curve a combination of one symmetric $S(H)$ and one antisymmetric $A(H)$ Lorentzian are used.

$$\begin{cases} S(H) = \dfrac{1}{\frac{1+(H_0-H_u)^2}{(\Delta H)^2}} \\[4mm] A(H) = \dfrac{\frac{H_0-H_{\text{res}}}{\Delta H}}{\frac{1+(H_0-H_u)^2}{(\Delta H)^2}} \end{cases} \qquad (4)$$

Therefore, the equation fits the curves is [2, 8]:

$$V = \frac{H_{\text{AC}}}{\Delta H} \left[2 V_s S(H) A(H) + V_a \left[A^2(H) - S^2(H) \right] \right] \quad (5)$$

where H_0 is the DC magnetic field applied in the sample, H_u is the effective field of magnetic anisotropy of thin film, V_a and V_s are the amplitudes of the antisymmetric and symmetric functions, respectively, H_{res} is the resonance magnetic field and ΔH is the line width of resonance. From the Eq. 5, two important parameters are obtained: the H_{res} and ΔH, which are used to determine Gilbert's damping coefficient of the LLG Equation.
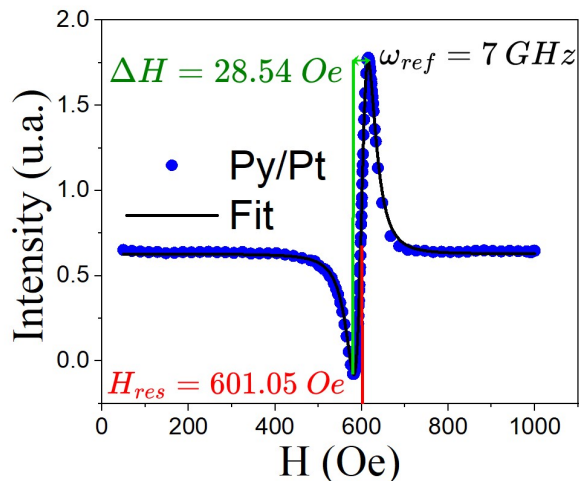

FIG. 7: Ferromagnetic resonance spectrum of the sample (Py (30 nm)/ Pt (6 nm)) recorded at 7.0 GHz. The blue circle represents the data and the black curve is the fitting using Eq. 5

The process of the FMR experiment was to put the sample on the waveguide with the thin film facing down to the waveguide, as seen in Figure 5c. Next, the frequency of RF (ω_{RF}) was fixed and varied the DC magnetic field (H_0) around the H_{res} to obtain a ferromagnetic resonance specter as see in Figure 7. Then data was fitted with Eq. 5 and found out the $\Delta H = (28.5 \pm 0.2)$ Oe and $H_{\text{res}} = (601.1 \pm 0.1)$ Oe for a determined ω_{RF}. These processes were done for each ω_{RF} in the range of between 3 and 8 GHz with the step of 1 GHz for Permalloy. For YIG, was done for ω_{RF} in the range of between 4 and 14 GHz with the step of 2 GHz.

E.   Inverse Spin Hall Effect (iSHE)

In the experiment of inverse Spin Hall Effect (iSHE), the goal was to measure the electric potential difference (ΔV), *i.e.* the iSHE, on the nonmagnetic material induced by an injection of pure spin current of the magnetic material using a spin pumping mechanism.

Then, the experiment configuration was almost the same as the FMR. However, two electrical contacts were placed on the sample (see Figure 8) to measure the ΔV using the lock-in amplifier. For the iSHE experiment, the modulation used was through the RF intensity and not through the AC magnetic field as performed in the FMR experiment.
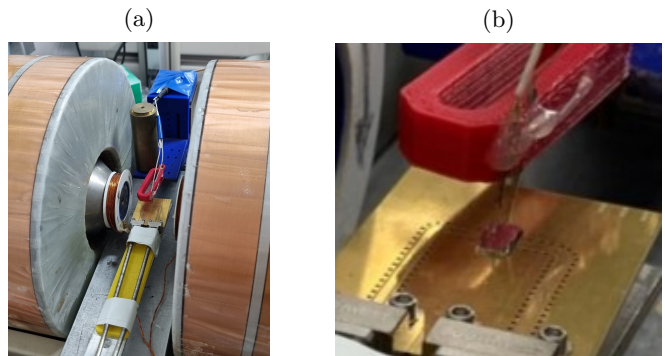
(a) (b)

FIG. 8: Photos of the experimental setup of inverse spin Hall effect. In (a) there is the electromagnetic with the electrical contacts. In (b) it is possible to see the two needles which contact the sample.

Therefore, the RF generator needs the capacity to generate a signal with sinusoidally modulated intensity at frequencies in the kHz range. The frequency of the modulation is the reference frequency (f_{ref}) to the lock-in amplifier. Then, from equation 3, the output signal is proportional to the input signal.

The process of the iSHE experiment was to put the sample on the waveguide with the thin film facing up because we measured the ΔV on the nonmagnetic material. Next, the electrical contacts were placed by lowering them onto the sample (see Figure 8b) and the resistance of the sample was measured using a multimeter through the same electrical contacts of the iSHE experiment on the sample to confirm the contact.

After, the $\omega_{\text{RF}} = 5$ GHz was fixed and varied the DC magnetic field (H_0) to obtain a graph of the $\Delta V \times H_0$, and 50 spectra were measured to calculate the mean.

III.   RESULTS AND DISCUSSION

A.   Gilbert's damping coefficient

We used the ferromagnetic resonance (FMR) to measure the Gilbert's damping coefficient (α) of different ferromagnetic (FM)/nonmagnetic (NM) thin films.

With the FMR line width (ΔH_0) for different resonance frequencies (f), obtained from the data analysis and adjustment of the FMR resultant curve, it is find a linear dependency between f and ΔH_0, and which will be used to calculate the damping coefficient (α).

Nonmagnetic material	Damping Coefficient FM/NM ($\alpha_{\text{FM/NM}} \times 10^{-3}$)
Ti	7.9 ± 0.1
Cu	9.0 ± 0.3
W	9.9 ± 0.1
Pt	10.3 ± 0.2

TABLE I: Gilbert's damping coefficient for different nonmagnetic material with the $Ni_{80}Fe_{20}$, or Permalloy, ferromagnetic material.

The relation between the angular coefficient of the $\Delta H_0 \times f$ curve and α is described by the Equation 6, where γ is the gyromagnetic constant and $\omega_{RES} = 2\pi \cdot f$. From this equation, is known that the value of α is the angular coefficient multiplied by a constant equal 2.802 GHz/kOe (or $\gamma/2\pi$). For each ferromagnetic/nonmagnetic film we have a specific angular coefficient and α. It is important to advise that the α is a dimensionless constant.

$$\Delta H_0 = \frac{\alpha}{\gamma}\omega_{\text{RF}} \qquad (6)$$

First, it was important to measure the damping coefficient for the 30 nm Permalloy film, and have it as a reference. We obtained a value of $\alpha_{\text{Py}} = (14.12 \pm 0.48) \times 10^{-3}$, and calculated the α for each Py/NM thin film, following the linear relations shown in Figure 9. The $\alpha_{\text{FM/NM}}$ final values are shown in Table I.
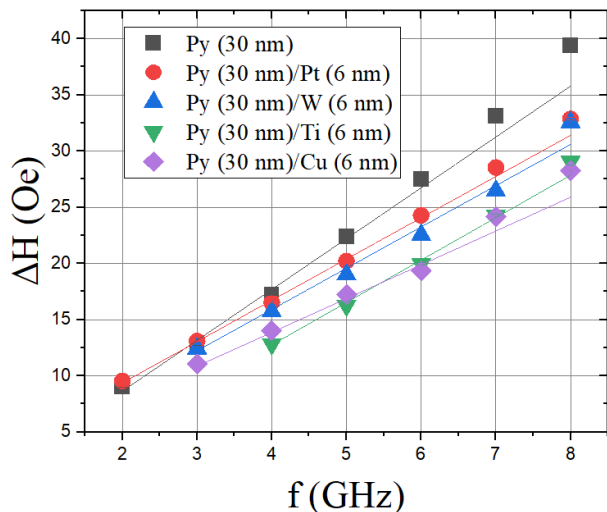
FIG. 9: ΔH and f relation for Py/NM thin films. The colors indicate different nonmagnetic materials: red for platinum, blue for tungsten, green for titanium and purple for copper. The Gilbert damping coefficient (α) were obtained by fitting the data with the Equation 6.
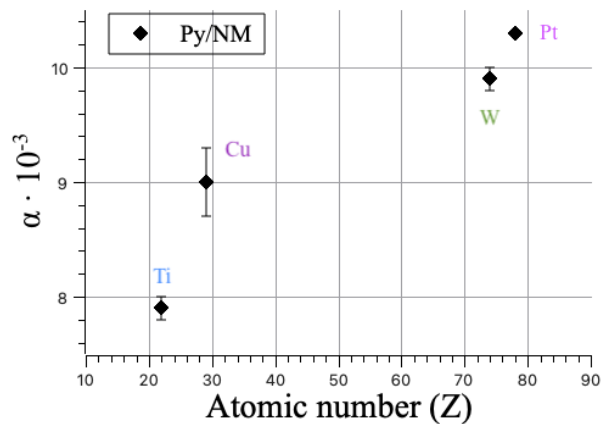
FIG. 10: Graph of α and atomic number (Z) relation for the different Py/NM thin films. The atomic numbers of each element are 22, 29, 74 and 78, for Ti, Cu, W and Pt respectively.

To understand why these materials (W and Pt) presented this behavior, was investigated by the graph of Figure 10 if the atomic number of each chemical element (Z) composing the nonmagnetic layer has any influence on the increase of the damping coefficient ($\alpha_{\text{FM/NM}}$). One can observe that the elements with higher atomic numbers also have a higher damping coefficient. That is because the atomic number is correlated to the spin-orbit coupling [3]. This coupling is responsible for generating a spin-flip scattering in the nonmagnetic material, producing a spin accumulation that contributes to the Gilbert damping enhancement. Thereby, heavier elements have larger spin-orbit coupling and consequently higher $\alpha_{\text{FM/NM}}$. However, the atomic number is not the only factor that influences $\alpha_{\text{FM/NM}}$, the conduction band electronic configuration of the nonmagnetic metal also contributes to its value.

1. Permalloy problem

According to the spintronics theory, the α values should be higher for the ferromagnetic/nonmagnetic ($\alpha_{\text{FM/NM}}$) thin films than for the bare ferromagnetic films (α_{FM}), such as Permalloy and YIG [4]. As shown in the results, this does not happen with the Py (30 nm) thin film, which presented a higher value than all the FM/NM thin films. When we compare the resultant value of $\alpha_{\text{Py}} = (14.12 \pm 0.48) \times 10^{-3}$ with the one presented in the literature [5], of approximately 7×10^{-3}, a high difference is seen between these values. Both discrepancies found between the values of α motivated us to study our sample of Permalloy.

The main factor that seems responsible for this increase in α may be the Permalloy oxidation. To confirm this hypothesis, first a new 30 nm Permalloy sample were fabricated, again using the magnetron sputtering. After,

the FMR technique was used to calculate a new α to this sample, and which appeared to be smaller than the first one (24 hours of air exposure). The values for both Permalloy samples are shown in Table II.

Air exposure time	Damping Coefficient Py (30 nm) ($\alpha \times 10^{-3}$)
0.5 hour	14.1 ± 0.5
24 hours	10.9 ± 0.1

TABLE II: Gilbert's damping coefficient for different samples of the Permalloy material, one with approximately 30 minutes of air exposure, and the other with 24 hours. This analysis shows us the α time dependence, such as the oxidation.

The analysis in Tab. II shows us that α_{Py}, as well as the material oxidation, seems to be time-related. The oxidation tends to increase over time, and the same happens with the Permalloy damping coefficient (α_{Py}).

The second method employed was the use of x-ray photoelectron spectroscopy (XPS), searching for more oxidation evidence. The obtained spectrum is shown in Figure 11. The oxygen presence is indicated by the different bonds of iron and nickel shown on the sample, indicating changes in the structure of the elements. A more detailed analysis can be done by doing spectroscopy of different depths of the Permalloy thin film, in order to investigate the thickness of the oxidation.
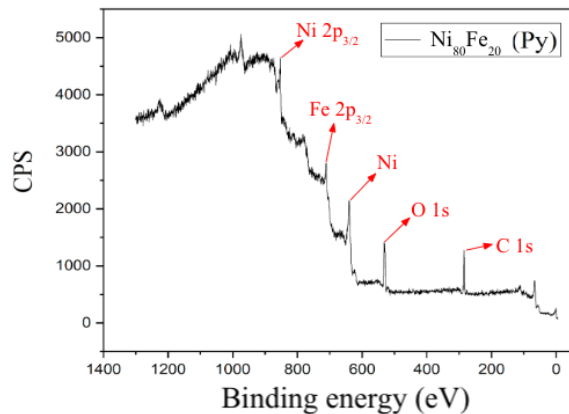

FIG. 11: Spectrum obtained via x-ray photoelectron spectroscopy (XPS). The bonds on the sample are indicated by the red writing. The Ni 2p$_{3/2}$ and Fe 2p$_{3/2}$ indicated bonds are both signs of the presence of oxygen.

In order to avoid the oxidation problem and estimate the α_{Py}, we analyzed the damping coefficient for different thicknesses of titanium as the nonmagnetic material. Titanium was as it presents the lowest $\alpha_{FM/NM}$ value, due to its atomic number. The Gilbert damping dependency of the thickness is shown in Figure 12.
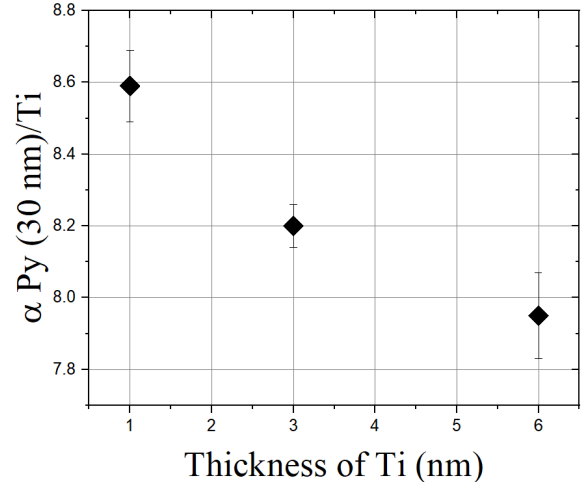

FIG. 12: Gilbert's damping coefficient (α) for different thickness of titanium.

When analyzing Fig. 12 it was observed that, even with the change in thickness, the α values do not vary significantly. This result allow us to use titanium as a type of "cap layer", as it does not have much of an impact on the damping coefficient value, and also assume the lowest value of titanium damping coefficient, $\alpha = 7.95 \times 10^{-3}$, as the standard value for Permalloy ($\alpha_{Py} = \alpha_{Py/Ti}$).

Assuming a α_{Py} value is important to subtract the ferromagnetic thin film contribution (α_{FM}) to the nonmagnetic material, and calculate the damping coefficient of the nonmagnetic materials (α_{SP}) only, as expected by the Equation 2. The values for α_{SP} of the nonmagnetic materials using $\alpha_{Py/Ti}$ as α_{FM} are shown in Table III.

Nonmagnetic material	Damping Coefficient ($\alpha_{SP} \times 10^{-3}$)
Cu	1.1 ± 0.3
W	2.0 ± 0.2
Pt	2.3 ± 0.3

TABLE III: Gilbert's damping coefficient for the nonmagnetic material, subtracting the Permalloy (ferromagnetic material) influence.

To better analyse the results shown and understand more about the materials and spintronics, we made thin films with YIG as the ferromagnetic material (instead of Permalloy). The two nonmagnetic materials with the higher $\alpha_{Py/NM}$ values, tungsten (W) and platinum (Pt), were deposited on YIG thin films. The YIG is interesting because, unlike Permalloy, it is an insulator material.

As we did for the Permalloy films, we constructed the FMR line width and frequency ($\Delta H \times f$) curves and calculated $\alpha_{FM/NM}$ for the YIG/nonmagnetic films. Here, we have two different thin films for each deposition (plat-

inum and tungsten), called as YIG V9 (for tungsten) and YIG V10 (for platinum). The linear relation for these films can be seen in Figure 13.
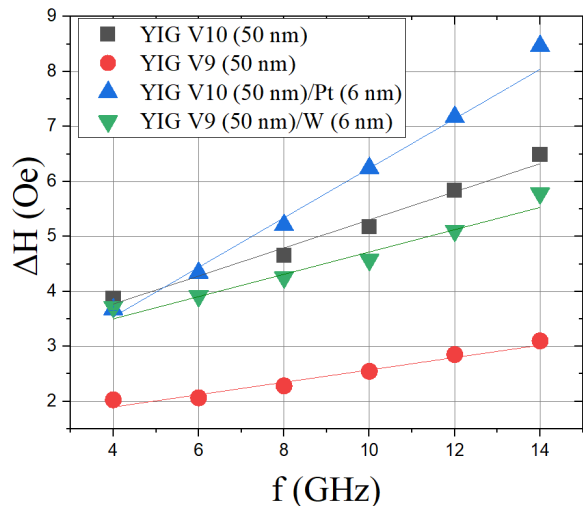

FIG. 13: ΔH and f relation for YIG/nonmagnetic thin films. The red and black dots indicate the YIG samples where the nonmagnetic layers were deposited, and the blue and green ones indicate the values for YIG/Pt and YIG/W thin films, respectively. The Gilbert damping coefficient (α) were obtained by fitting the data with the Equation 6.

Following the results for the Permalloy/nonmagnetic materials, we applied the Equation 2 for the YIG/nonmagnetic samples, obtaining the α_{SP} when using YIG as the ferromagnetic material. Once we know the damping coefficient for ours YIG samples (YIG V9 and YIG V10), and which are equal $\alpha_{YIG\ V9} = 0.32 \pm 0.03$ and $\alpha_{YIG\ V10} = 0.73 \pm 0.06$, the α_{SP} for tungsten and platinum can be seen in Table IV.

Nonmagnetic material	Damping Coefficient ($\alpha_{SP} \times 10^{-3}$)
W	0.25 ± 0.07
Pt	0.61 ± 0.09

TABLE IV: Gilbert's damping coefficient for the nonmagnetic material, subtracting the YIG (ferromagnetic material) influence.

When analysing all the results, it is evident that the tungsten and platinum are the nonmagnetic materials with higher Gilbert's damping coefficient increase, and consequently will generate more spin-current. Additionally, YIG appears to be better for spin current injection since the oxidation problem can occur in the Py and it is prevented in the YIG which is already an oxide.

B. Inverse Spin Hall Effect (iSHE)

The inverse Spin Hall Effect (iSHE) of the Py (30 nm)/Pt (6 nm) was measured seen in Figure 14. However, the graphics are not as expected from a Lorentzian as described by K. Ando *et. al* [9].
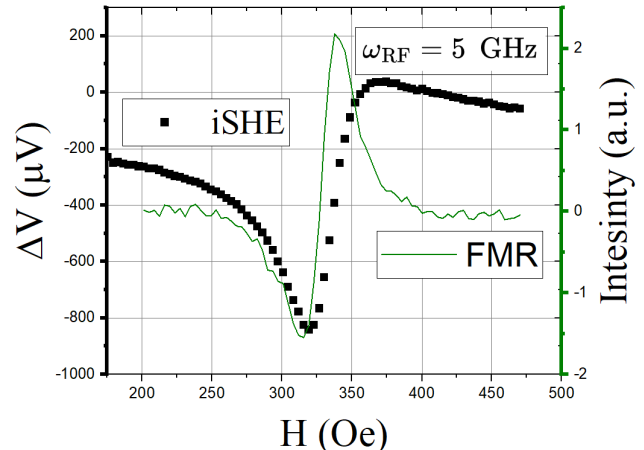

FIG. 14: Graph of iSHE of the Py(30 nm)/Pt(6 nm). In black is the experimental data of the iSHE experiment and the green curve is the FMR showing that the sample is in the resonance region.

Then, considering the sample of Py (30 nm)/Ti (6 nm) with our reference for Py (30 nm) as previously discussed in (III A 1). The iSHE of the Py (30 nm)/Ti (6 nm) was measured (see Figure 15). We inferred that it is an antisymmetric signal intrinsic due to an additional contribution of the Py anisotropic magnetoresistance (AMR) [10].
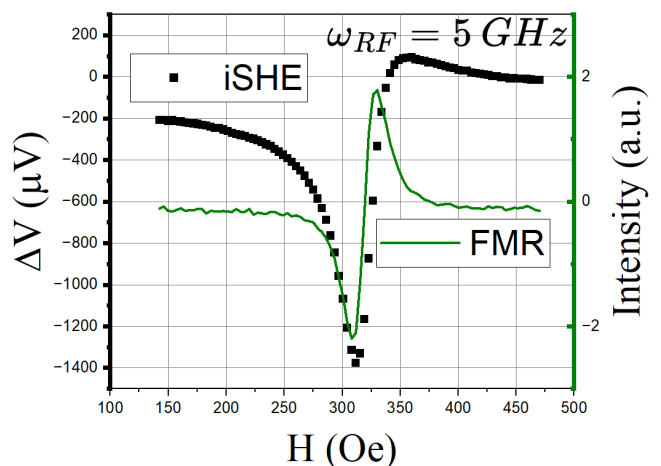

FIG. 15: Graph of iSHE of the Py (30 nm)/Ti (6 nm) . In black is the experimental data of the iSHE experiment and the green curve is the FMR showing that the sample is in the resonance region.

Therefore, this means that the measured of the Py(30 nm)/Pt(6 nm) has two contributions one is the symmetric signal from iSHE and another antisymmetric signal from the Py AMR [10].
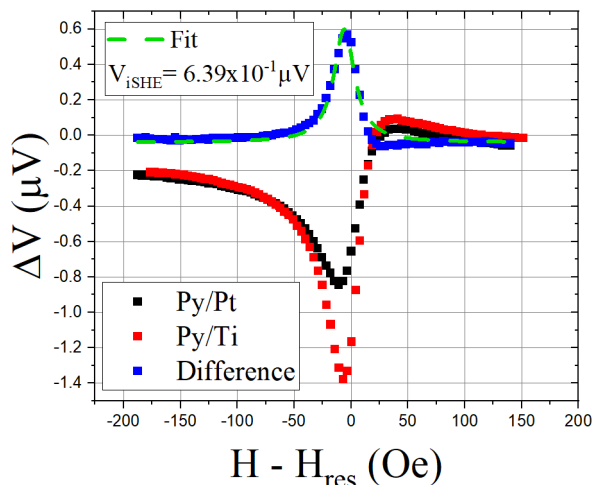

FIG. 16: Graph of the Py(30 nm)/Pt(6 nm) (in black) and Py(30 nm)/Ti(6 nm) (in red) of iSHE experiment for $\omega_{\rm RF} = 5$ GHz. In blue is the difference between the experimental data of the Py/Pt and Py/Ti and in green is the fit of the Lorentzian..

Thus to find out only the signal from iSHE the difference was calculated between $\Delta V_{\rm Py/Pt}$ and $\Delta V_{\rm Py/Ti}$ obtaining a graph as seen in Fig. 16 after a Lorentzian was adjusted obtained the $\Delta V_{\rm iSHE}$ and the same process was done for Py (30 nm)/W (6 nm). For both samples, the results are shown in Table V.

Sample	ΔV_{iSHE} (μV)
Py (30 nm)/Pt (6 nm)	$(6.4 \pm 0.2) \times 10^{-1}$
Py (30 nm)/W (6 nm)	$(5.2 \pm 0.2) \times 10^{-1}$

TABLE V: The values of ΔV_{iSHE} for sample with Py.

From Table V is inferred that the iSHE of the Py/Pt is greater than Py/W. The results are coherent with $\alpha_{\rm Pt}$ is greater than $\alpha_{\rm W}$.

In the next step, the sample YIG/Pt was measured (see Fig. 17) in which the graph presents the expected Lorentzian function. We inferred that it occurs because the YIG is an electrical insulator. So YIG did not have an intrinsic antisymmetric sign due to the anisotropic magnetoresistance (AMR). Then, a Lorentzian was fitted obtaining the value of $\Delta V_{\rm iSHE}$, the same process was done for YIG/W and the results are in Table VI.

Moreover, we plotted a graph with YIG/Pt and YIG/W together (see Fig. 18) to compare the results. From Fig. 18 and Table VI was noticed that the ΔV of YIG/Pt was greater than the YIG/W. The results are
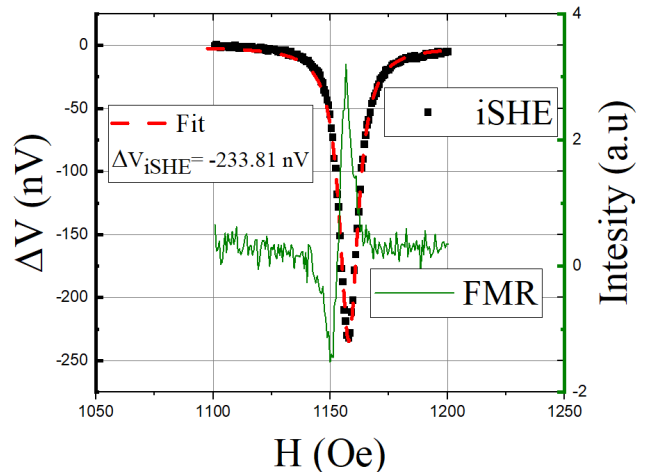

FIG. 17: Graph of iSHE of the YIG (50 nm)/Pt (6 nm) for $\omega_{\rm RF} = 5$ GHz. In black is the experimental data of the iSHE experiment, the dash curve in red is the fit of Lorentzian and the green curve is the FMR showing that the sample is in the resonance region.

Sample	$\Delta V_{\rm iSHE}$ (nV)
YIG (50 nm)/Pt (6 nm)	-233.8 ± 0.1
YIG (50 nm)/W (6 nm)	41.4 ± 0.2

TABLE VI: The values of $\Delta V_{\rm iSHE}$ for sample with YIG.

coherent, because $\alpha_{\rm Pt}$ is greater than $\alpha_{\rm W}$.

Furthermore, the signal of the $\Delta V_{\rm iSHE}$ of the YIG/Pt is opposite of the YIG/W because the total spin and orbital moments interact through the spin-orbit coupling is described by the equation [11]:

$$W_J = \lambda \mathbf{L} \cdot \mathbf{B} \tag{7}$$

where $\boldsymbol{S}$ is total spin moment and $\boldsymbol{L}$ is total orbital moment and λ is the spin-orbit coupling constant. The λ is positive when the shell is less than half-full or is negative when the shell is more than half-full.

By Hund's law, the platinum (Pt) last shell is more than half-full ($\lambda_{\rm Pt} < 0$), however, the tungsten (W) last shell is less than half-full ($\lambda_{\rm W} > 0$). The $\lambda_{\rm Pt}$ and the $\lambda_{\rm W}$ have opposite signals, so Pt and W tend to scatter electrons in opposite directions concentrating electrons on opposite sides, generating the opposite sign of $\Delta V_{\rm iSHE}$.

C.   Internet of things

As an additional but relevant topic in the research process, it can be noted that interdisciplinary work can support physics research. Within the experimental process, it was observed that various instruments depend on cooling or other requirements for their optimal and/or correct
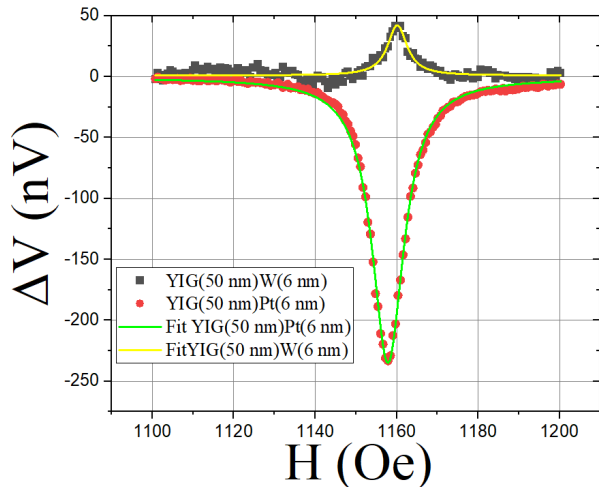
FIG. 18: Graph of iSHE of the YIG/Pt and YIG/W for $\omega_{\mathrm{RF}} = 5$ GHz. In gray is the experimental data of the YIG/W, and in red is the experimental data of the YIG/Pt. The curve in yellow is the fit of Lorentzian of YIG/W and the curve in green is the fit of Lorentzian of YIG/Pt.

FIG. 19: Image of ferromagnetic resonance (FMR) machine in the laboratory with the water supply connected.

operation. Therefore, in response to this situation, a solution based on IoT was proposed as a contribution and legacy for the laboratory and Brazilian Center of Physical Research (CBPF).

1. Problem Statement

The ferromagnetic resonance (FMR) equipment requires a continuous water supply for coil cooling. Consequently, any interruption in the water flow may delay measurements and potentially damage components. Given that this is a costly asset requiring constant monitoring, monitoring the continuous water supply to the FMR was identified as an important problem to be addressed. It can see in the Fig. 19.

2. Proposed Solution

To address the issue of monitoring the water flow used for cooling the FMR, main components it was considered for the monitoring system's prototype would consist of a sensor for water flow measurement, a microcontroller to receive the signal from the sensor and obtain the measured value, and subsequently take action based on the presence or absence of water flow.

3. Prototype

For the prototype, it was chosen a hall-effect sensor YF-S201, which features a rotor that sends out a sig-

nal for each rotation. Also, through a conversion equation and measurement interval, these pulses can be interpreted to obtain the average water flow within the interval.

Additionally, an ESP8266 microcontroller programmed in micropython was utilized. The ESP8266 receives and interprets sensor signals to obtain the measured flow value, and it is equipped with two LEDs to visually indicate the presence or absence of water flow.

As the prototype was intended solely for this FMR machine, it was decided that the microcontroller would be programmed to process the measured value directly and, depending on whether water flow is not detected, it would send out an alert via email using the SMTP communication protocol to notify that the sensor has not detected water. The complete diagram is in Fig. 20 and the prototype can be seen in Fig. 21.

Furthermore, the YF-S201 sensor and ESP8266 microcontroller were chosen for their low cost, as well as the ESP8266's versatility in programming, not limited to micropython.
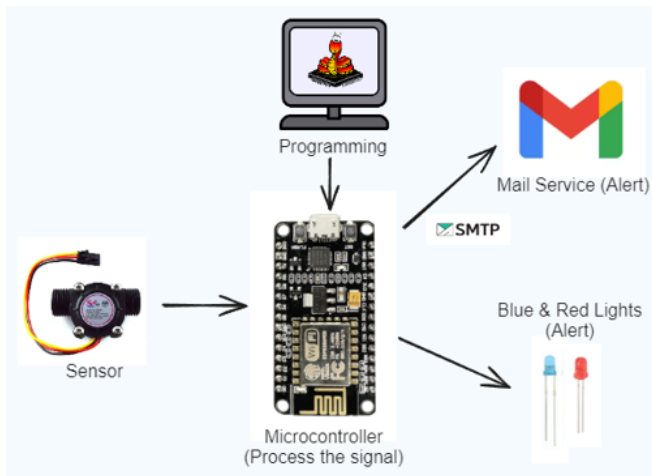
FIG. 20: Prototype diagram for monitoring the continuous water supply to the FMR machine.
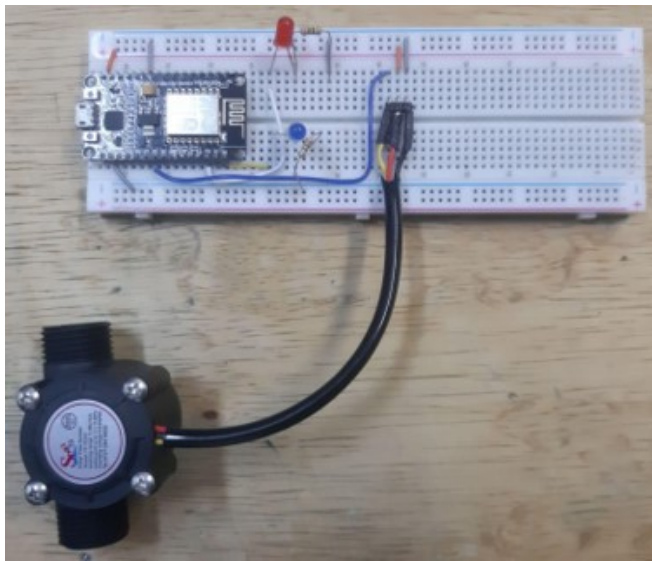

FIG. 21: Prototype for monitoring the continuous water supply to the FMR machine.

4. Potential Future Implementations

The prototype shown effectively monitors water flow and fulfills its primary objective. However, this system could be extended or adapted to various laboratory equipment requiring monitoring of different indicators.

Moreover, the architecture could be modified to transition to a structure based on the use of IoT agents for controlling multiple sensors placed on various instruments and machinery within the institution. These agents would handle sending information to a centralized system equipped with dashboards, achievable through technologies such as Fiware or Grafana. Additionally, the system could be enhanced with more granular alert systems using open-source technologies like Camunda.

IV. CONCLUSION

In this article, four nonmagnetic materials deposited on Permalloy were investigated to facilitate the development of efficient spintronic devices. In this context, through the analysis of the obtained results, it was possible to conclude that the most efficient materials were platinum and tungsten due to the high spin-orbit coupling present– a phenomenon whose correlation with the high atomic number of these materials had also been observed. However, it was not feasible to adequately compare the contribution to the variation of the Gilbert damping parameter, as the results from the pure Permalloy sample were discrepant from those in the literature. This discrepancy could be attributed to the oxidation present on the material's surface, which was detected through XPS. On the other hand, YIG proves to be a more promising FM substrate for spintronic applications due to its low Gilbert damping and absence of conductivity, which prevents the voltage loss observed in Permalloy films. Furthermore, it was observed that the iSHE measurements of YIG/Pt and YIG/W samples exhibited opposite signals due to the opposite spin-orbit interactions that results in an opposite scattering for electrons with the same spin in these materials. Therefore, among the studied multilayer films, YIG/Pt exhibited the best spin current injection among the studied bilayers.

[1] K. J. M. Gilbert, T. L., Anomalous rotational damping in ferromagnetic sheets, American Institute of Electrical Engineers , 253 (1955).

[2] R. Torrão, *Estudo da dinâmica de magnetização em sistemas FM/NM para aplicações em spintrônica*, Dissertação de mestrado (2019).

[3] Y. Tserkovnyak, A. Brataas, and G. E. W. Bauer, Spin pumping and magnetization dynamics in metallic multilayers, Physical Review B **66**, 10.1103/physrevb.66.224403 (2002).

[4] Y. Tserkovnyak, A. Brataas, and G. E. W. Bauer, Enhanced gilbert damping in thin ferromagnetic films, Phys. Rev. Lett. **88**, 117601 (2002).

[5] Y. Zhao, Q. Song, and S. Yang, Experimental investigation of temperature-dependent gilbert damping in permalloy thin films., Sci Rep 6 (2016).

[6] W. Kuch, Ferromagnetic resonance (fmr) (2019).

[7] J. H. Scofield, Frequency-domain description of a lock-in amplifier, American Journal of Physics **62**, 129 (1994).

[8] A. M. Gonçalves, *Dinâmica da magnetização em sistemas spintrônicos: CoFeB/MgO e Py/Cu/Pt*, Tese de doutorado (2015).

[9] K. Ando, S. Takahashi, J. Ieda, Y. Kajiwara, H. Nakayama, T. Yoshino, K. Harii, Y. Fujikawa, M. Matsuo, S. Maekawa, and E. Saitoh, Inverse spin-hall effect induced by spin pumping in metallic system, Journal of Applied Physics **109**, 10.1063/1.3587173 (2011).

[10] O. Mosendz, V. Vlaminck, J. E. Pearson, F. Y. Fradin, G. E. W. Bauer, S. D. Bader, and A. Hoffmann, Detection and quantification of inverse spin hall effect from spin pumping in permalloy/normal metal bilayers, Phys. Rev. B **82**, 214403 (2010).

[11] A. P. Guimarães, *Magnetismo e Ressonância Magnética em Sólidos* (EDUSP, 2009).